

PHYSICS

Quasi-1D exciton channels in strain-engineered 2D materials

Florian Dirnberger¹, Jonas D. Ziegler², Paulo E. Faria Junior³, Rezlind Bushati^{1,4}, Takashi Taniguchi⁵, Kenji Watanabe⁶, Jaroslav Fabian³, Dominique Bougeard², Alexey Chernikov^{2,7*}, Vinod M. Menon^{1,4*}

Strain engineering is a powerful tool in designing artificial platforms for high-temperature excitonic quantum devices. Combining strong light-matter interaction with robust and mobile exciton quasiparticles, two-dimensional transition metal dichalcogenides (2D TMDCs) hold great promise in this endeavor. However, realizing complex excitonic architectures based on strain-induced electronic potentials alone has proven to be exceptionally difficult so far. Here, we demonstrate deterministic strain engineering of both single-particle electronic bandstructure and excitonic many-particle interactions. We create quasi-1D transport channels to confine excitons and simultaneously enhance their mobility through locally suppressed exciton-phonon scattering. Using ultrafast, all-optical injection and time-resolved readout, we realize highly directional exciton flow with up to 100% anisotropy both at cryogenic and room temperatures. The demonstrated fundamental modification of the exciton transport properties in a deterministically strained 2D material with effectively tunable dimensionality has broad implications for both basic solid-state science and emerging technologies.

INTRODUCTION

On-demand accessibility of excitonic quantum many-body phases promises a leap toward next-generation quantum optoelectronics (1, 2). The rich variety of excitonic many-body states, including insulators (3, 4), superfluids (5, 6) and condensates (7), electron-hole liquids (8, 9), and superconductive (10) and ferromagnetic phases (11), offers exceptional opportunities to implement concepts of the Hubbard model and other quantum simulators (2, 12–16) searching for suitable material platforms. In the key challenge of artificially tailoring the properties of excitonic systems toward supporting such exotic phases, strain engineering has been established as one of the most powerful techniques at hand (1, 17–19). Due to reduced dielectric screening and strong Coulomb correlations, two-dimensional transition metal dichalcogenides (2D TMDCs) are a highly promising platform for room temperature implementations of these concepts. Notably, their van der Waals (vdW) nature further allows complex nanoscale strain architectures to be readily implemented with essentially arbitrary geometry, a degree of freedom in the design of quantum simulators comparable to lithographically defined superconducting circuits (2). In addition, while most studies concentrated on funneling excitons (20–23) or free electrons (24) into localized potential minima, recent reports (25, 26) suggest promising perspectives to manipulate the mobility of excitons via strain tuning. This provides a strong motivation to build

strain-induced quasi-1D potentials for mobile exciton quasiparticles in an otherwise fully 2D system.

In this work, we demonstrate deterministic strain engineering of excitonic many-particle interactions, allowing to substantially enhance localization of excitons in one direction and their mobility in another. Merging 1D semiconductor nanowires with WSe₂ monolayers into hybrid heterostructures, we create artificial strain-induced exciton transport channels in the 2D matrix. These are found to exhibit near 100% anisotropy in the exciton flow not only at cryogenic but also at room temperatures. The underlying changes in the local multivalley bandstructure are shown to strongly affect both confinement and dynamical motion of excitons, leading to their enhanced mobility within the channel. Our approach introduces a highly tunable platform to modify the effective dimensionality of the exciton motion while fully retaining strong Coulomb and light-matter interaction of the pristine 2D material.

RESULTS

Strain-engineered quasi-1D confinement potentials

Our hybrid 1D/2D structure is schematically illustrated in Fig. 1A. The active component that hosts excitons is a monolayer (1L) WSe₂, fully encapsulated in high-quality hexagonal BN (hBN) to provide uniform dielectric screening and suppress disorder. The hBN-WSe₂ stack is then placed on top of a GaAs/Al_{0.36}Ga_{0.64}As core/shell nanowire and is deformed to a 90-nm height over a length of about 8 μm, as shown by the atomic force microscopy image in Fig. 1B. This mechanical deformation with several 100-nm width leads to a pronounced spatial dependence of the spectral characteristics of 1L WSe₂. A series of micro-photoluminescence (μ-PL) scans, recorded along the transverse *y* direction with respect to the nanowire axis at *T* = 4 K, is plotted both as-measured and deconvoluted by the optical resolution on the right and left sides of Fig. 1C, respectively. The data show a pronounced shift of the extracted bright exciton resonance (*X*₀) as a function of the spatial coordinate *y*. Extended spectra are presented in Fig. 1D, plotted relative to the *X*₀ energy. Following the

Copyright © 2021
The Authors, some
rights reserved;
exclusive licensee
American Association
for the Advancement
of Science. No claim to
original U.S. Government
Works. Distributed
under a Creative
Commons Attribution
NonCommercial
License 4.0 (CC BY-NC).

¹Department of Physics, City College of New York, New York, NY 10031, USA.

²Department of Physics, University of Regensburg, 93040 Regensburg, Germany.

³Institute for Theoretical Physics, University of Regensburg, 93040 Regensburg, Germany.

⁴Department of Physics, The Graduate Center, City University of New York, New York, NY 10016, USA.

⁵International Center for Materials Nanoarchitectonics, National Institute for Materials Science, Tsukuba, Ibaraki 305-004, Japan.

⁶Research Center for Functional Materials, National Institute for Materials Science, Tsukuba, Ibaraki 305-004, Japan.

⁷Dresden Integrated Center for Applied Physics and Photonic Materials (IAPP) and Würzburg-Dresden Cluster of Excellence ct.qmat, Dresden University of Technology, Dresden 01187, Germany.

*Corresponding author. Email: alexey.chernikov@tu-dresden.de (A.C.); vmenon@ccny.cuny.edu (V.M.M.)

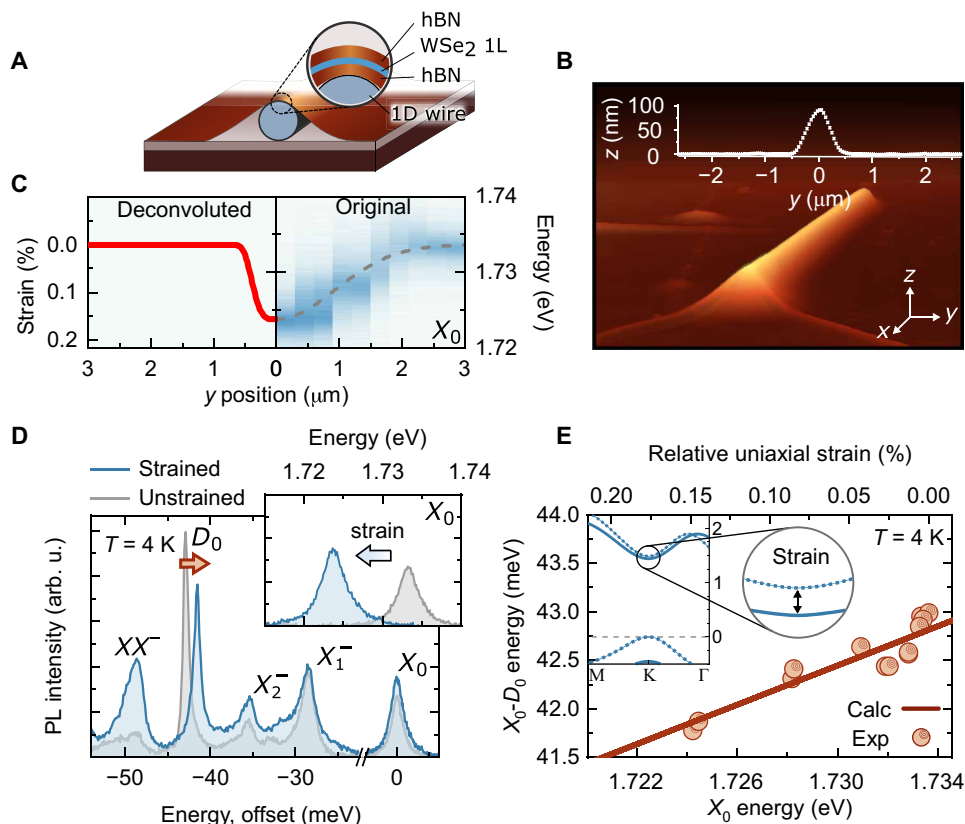


Fig. 1. Strain-engineered energy landscape in a hybrid 1D/2D structure. (A) Schematic illustration of the sample structure. (B) Topographic atomic force microscopy image (inset: lateral height profile from the center). (C) Measured energy of the exciton emission of 1L WSe₂ in a false-color plot as a function of the spatial coordinate perpendicular to the nanowire direction. Shown are as-measured data (right) and a convolution of a super-Gaussian strain profile (left) with the optical collection spot (gray dashed line). (D) Extended micro-photoluminescence (μ -PL) spectra of strained and unstrained regions as a function of the relative energy with respect to the X_0 resonance (inset: X_0 spectra plotted on absolute energy axis). (E) Measured and calculated energy splitting between bright (X_0) and spin-dark (D_0) excitons as a function of the X_0 peak energy (inset: first-principles electronic band structure of an unstrained 1L WSe₂, dashed and solid lines represent bands with different spin). Data in (C) to (E) were obtained at $T = 4$ K.

deformation, all detected emission features of 1L WSe₂, including dark states and higher-order complexes, shift accordingly (also see note S1).

The absence of changes in the energy splitting between the exciton ground and excited states, as well as charged states detected in reflectance (see note S3), confirms uniform dielectric screening and doping in the structure. In particular, the high exciton binding energy of pristine hBN-encapsulated 1L WSe₂ on the order of 180 meV is kept unchanged across the channel.

From spectral analysis, we thus unambiguously identify uniaxial strain induced by the nanowire in the mechanically deformed WSe₂ as the main cause for the local changes in the exciton energy landscape. The absence of additional spectral broadening of the X_0 emission peak observed in the center of the deformation in Fig. 1D indicates a largely uniform strain distribution within the μ -PL collection spot. To quantify the resulting potential from spectral observables, we use a super-Gaussian profile, also shown in Fig. 1C, which accurately approximates the spatially broadened X_0 energy profile after convolution with the optical collection spot. To determine strain, we use a gauge factor from first-principles calculations of -63.2 meV per % strain for the absolute shift of the bandgap. This scaling is largely consistent with reported room temperature values for 1L

WSe₂ (25–27). Therefore, we obtain a strain value of 0.15%, resulting in an attractive potential perpendicular to the nanowire direction with a depth on the order of 10 meV. A detailed discussion of the strain profile analysis in our samples is provided in note S4.

Within the rich emission spectrum of 1L WSe₂, recent first-principles calculations predicted a subtle yet uniquely characteristic fingerprint of strain, a shift between spin-allowed bright X_0 and spin-forbidden dark D_0 states (28, 29). As apparent from Fig. 1E, we observe a continuous reduction of the $X_0 - D_0$ energy separation recorded in μ -PL scans across the deformation (cf. also Fig. 1D). It is consistent with the interpretation of strain determining the absolute shift of the exciton resonances in our samples. Quantitatively, the relative shift between X_0 and D_0 agrees with the value of -6.4 meV per % strain predicted from first-principles calculations (see notes S2 and S4).

The resulting potential minimum enhances the local exciton density, as evidenced by the increase of charged biexciton emission (see XX^- in Fig. 1D and note S5), and strongly affects the exciton propagation. All results presented in the manuscript were obtained from this device. Measurements conducted on several different devices on two separate hBN-encapsulated WSe₂ flakes confirm all main conclusions and are presented in note S6.

Unidirectional exciton propagation at low temperature

We directly monitor the spatially resolved exciton dynamics through transient microscopy using pulsed optical excitation of the hybrid 1D/2D structure and detect the luminescence with a streak camera. Representative profiles of the exciton emission are presented in Fig. 2 (A and B) along the direction parallel (x) and perpendicular (y) to the potential channel induced by the nanowire. Along the channel, we observe characteristic spatial broadening of the emission over time from the expanding cloud of mobile excitons. In stark contrast to that, propagation perpendicular to the nanowire direction appears to be entirely suppressed.

To quantify these observations, emission profiles at different times after the excitation are fitted with Gaussian functions, as illustrated in Fig. 2 (A and B). The resulting, time-dependent values of the variance, $\Delta\sigma(t)^2$, are presented in Fig. 2C for the two directions as well as in comparison to the measurements from an unstrained sample region. Along the confinement channel, $\Delta\sigma(t)^2$ increases linearly with time, characteristic for diffusive propagation. The diffusion coefficient $D_x = 1.4 \pm 0.1 \text{ cm}^2/\text{s}$, extracted from the slope via $\Delta\sigma(t)^2 = 2Dt$, is comparable to the values in pristine, unstrained sample positions and is in reasonable agreement with low-temperature diffusion coefficients in hBN-encapsulated WSe₂ (30). In contrast, the extracted effective diffusivity vanishes almost completely in the transverse direction, yielding $D_y = 0.1 \text{ cm}^2/\text{s}$. The associated degree of anisotropy, $(D_x - D_y)/(D_x + D_y)$, is as high as 86%, emphasizing strongly directional exciton propagation along the strain-induced channel. Here, we note that the determined anisotropy is fully reproducible across several devices and is very robust with respect to the excitation density (notes S6 and S8). Moreover, the PL in strained and unstrained regions of the monolayer exhibits very similar decay dynamics and can therefore not result in any anisotropy for the diffusion of excitons (see note S7).

It is interesting to consider that, particularly at very low temperatures, the confinement energy of 10 meV should be fully sufficient

to capture and constrain the excitons. To estimate the impact of such a strain potential, we simulate the exciton dynamics in our hybrid 1D/2D structure by constructing an attractive quasi-1D potential $u = u(\mathbf{r})$ based on the experimentally determined values for the strain profile and diffusion behavior from the unstrained area, as schematically illustrated in Fig. 3A. As excitons propagate diffusively inside the channel, even along y (see note S9), we characterize their motion by an isotropic diffusion coefficient D . A spatially and time-resolved exciton density $n = n(\mathbf{r}, t)$ then evolves according to

$$\frac{\partial n}{\partial t} = D\Delta n + \frac{D}{k_b T}(\nabla n \cdot \nabla u + n\Delta u) - \frac{n}{\tau} \quad (1)$$

The first term on the right-hand side accounts for diffusive-free propagation, the second term arises from drift induced by the potential gradient, and the third term represents population decay (see Materials and Methods).

Simulated maps of the exciton density are presented in the top panels of Fig. 3B, normalized at each time delay. The simulation clearly shows that the excitons injected from the 2D reservoir progressively adapt to the strain-induced confinement potential over time. While localized perpendicularly to the channel, the excitons are predicted to diffuse along the channel direction, supporting our observation of a highly anisotropic transport. For comparison, time-resolved 2D images of the measured emission are presented in the bottom panels of Fig. 3B, obtained by manually scanning the detected segment of the image along the x direction. The experiment shows the development of an increasingly elongated shape of the exciton emission over time after an initially symmetric distribution.

Room temperature diffusion anisotropy

Following the discussion of highly anisotropic exciton transport at cryogenic temperatures, we now demonstrate that the observed high degree of propagation anisotropy is sustained even at room temperature. The measured time-dependent variance, $\Delta\sigma(t)^2$, of the exciton distribution is presented in Fig. 4A along and across the strain-induced channel at $T = 290 \text{ K}$. Similar to our observations at $T = 4 \text{ K}$, we detect efficient diffusion along the nanowire direction with $D_x = 13.5 \pm 1 \text{ cm}^2/\text{s}$ (corresponding to an effective mobility of $540 \text{ cm}^2/\text{Vs}$) and a diffusivity across the channel being close to zero. The latter even exhibits a small, negative value of $D_y = -0.8 \pm 0.1 \text{ cm}^2/\text{s}$, attributed to the shrinking of the exciton distribution. The possible impact of exciton funneling is further discussed in note S5. We note that measurements on a second nanowire-induced deformation confirm the strong dependence on the direction of the exciton transport, while showing a diffusion of $D_y = 0 \text{ cm}^2/\text{s}$ across the strain potential (see note S4). Experimentally, we thus effectively observe 100% anisotropy in the exciton propagation.

Considering the average thermal energy of the excitons on the order of 25 meV, the confinement potential alone should not lead to such a strong difference in effective diffusion coefficients (note S10). Here, a crucial feature of our hybrid 1D/2D platform comes into play: The excitons not only experience a spatially dependent change in their total energy but also in their momentum scattering rate. As our measurements presented in Fig. 4B show for bright excitons, in agreement with recent reports (25, 26, 31, 32), a reduction of intervalley exciton-phonon scattering and the associated increase in exciton coherence occur under strain due to substantial energy shifts across the multivalley band structure. This leads to the very peculiar scenario schematically illustrated in Fig. 4B—an emergence of a

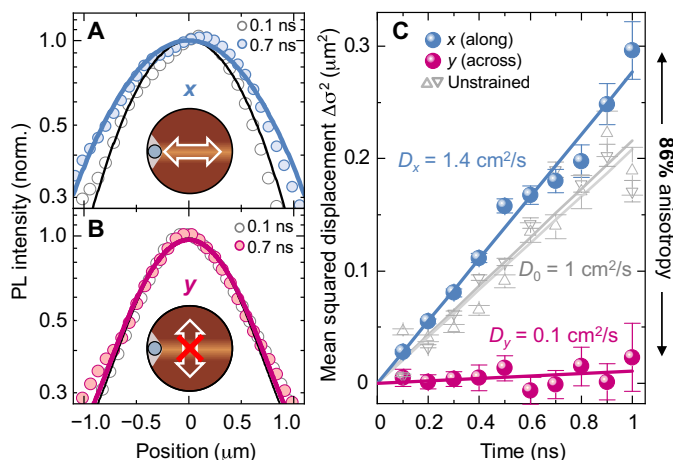


Fig. 2. Anisotropic exciton diffusion at $T = 4 \text{ K}$. (A) Spatially resolved exciton emission profiles obtained along the confinement channel direction (x), presented immediately after the excitation and at a later time of 0.7 ns. Gaussian fits are shown by solid lines. (B) Corresponding emission profiles measured across the channel (y). (C) Extracted time-dependent variance of the exciton distribution together with the data from the unstrained region. Error bars denote the SE of the Gaussian fits at each time step. Corresponding diffusion coefficients from $\Delta\sigma(t)^2 = 2Dt$ and the resulting degree of anisotropy are indicated.

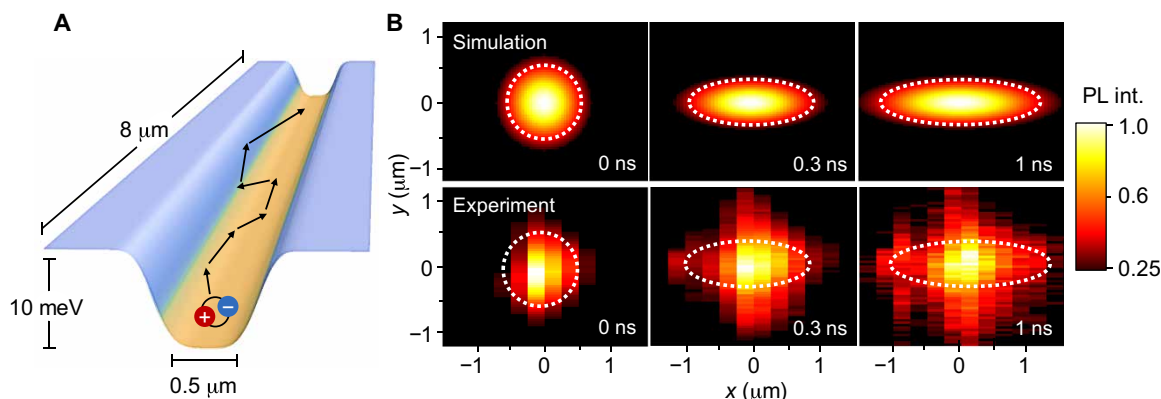


Fig. 3. 2D imaging of the transient exciton distribution at $T = 4$ K. (A) Schematic illustration of the anisotropic diffusion along the quasi-1D channel. (B) Top: Simulated images of the 2D exciton density $n(r, t)$ at different times after injection at the center of the potential well. Bottom: Corresponding experimentally obtained images of the exciton emission. Dashed lines are guides to the eye.

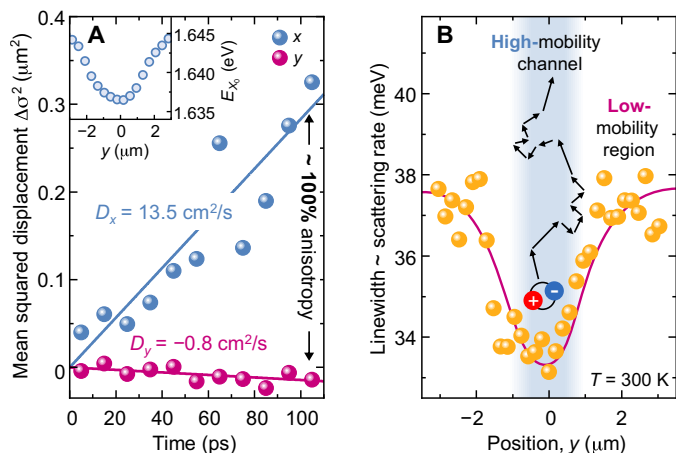


Fig. 4. Room temperature anisotropy in the exciton propagation. (A) Time-dependent variance of the exciton distribution along (x) and across (y) the strain-induced channel at $T = 290$ K. Inset: Exciton emission energy as function of the y coordinate. (B) Spectral linewidth of the exciton resonance corresponding to a spatially dependent scattering rate at room temperature. Data points are extracted from individual PL spectra recorded along y . The background schematically illustrates exciton propagation in a channel with comparatively weak scattering (high mobility) surrounded by regions of efficient scattering (low mobility). The blue-shaded region approximates the width of the channel based on the underlying strain profile.

channel with suppressed scattering, favoring exciton propagation. This channel is surrounded by unstrained 1L WSe₂ with effectively lower mobility (also see note S10). This unique combination of strain-dependent scattering and coherence with an external confinement potential ultimately results in a highly anisotropic exciton transport at room temperature.

DISCUSSION

The demonstrated capability to deterministically guide neutral light-emitting quasiparticles along predefined pathways up to room temperature provides a particularly promising platform for the design of excitonic architectures and networks. The hybrid 1D/2D strain-based approach fully preserves the benefits of strong light-matter interactions and highly stable excitons of the 2D

TMDC. Our platform should thus be highly attractive for controlling excitons in a broad variety of other low-dimensional structures, including vdW heterostructures designed to host interlayer (33) or Moiré-like excitations (34). While strain-induced mobility enhancement and highly directional exciton transport with near 100% anisotropy at room temperature promise compelling advantages for exciton-based applications at ambient conditions, one can also anticipate fascinating low-temperature physics for channel widths smaller than about 60 nm (see note S9). Such strain-induced hybrid channels—highly promising to reach truly 1D regimes—may pave the way toward mesoscopic quantum transport phenomena of correlated many-body states, merging continuously tunable dimensionality with novel quasiparticle physics (35).

MATERIALS AND METHODS

Sample fabrication

The hybrid 1D-2D devices illustrated in Fig. 1A were assembled in a layer-by-layer bottom-up approach. First, standard SiO₂/Si substrates (oxide thickness, 285 nm) were cleaned using a high-intensity ultrasonic bath in acetone and propan-2-ol for 2 min each and a subsequent blow dry using N₂. To remove remaining adsorbates, the samples underwent an O₂ plasma cleaning for 5 min at 200 W. Epitaxially grown GaAs/Al_{0.36}Ga_{0.64}As core/shell nanowires, with 80 ± 9 nm diameter and a length of 8 ± 1 μm, were then deposited by bringing the as-grown nanowire wafer into mechanical contact with a clean SiO₂/Si substrate (36).

Several hBN-encapsulated WSe₂ heterostructures were fabricated as follows: hBN crystals supplied by colleagues from National Institute for Materials Science (NIMS, Tsukuba) were cleaved and thinned down using two sheets of “Scotch Magic Tape.” One of the tapes was then placed on polydimethylsiloxane (PDMS; WF-20-X4, Gel-Pak) without adding additional pressure. A suitable, few-nanometer-thin hBN layer was chosen by its optical contrast and then stamped on top of several nanowires using a home-built sample holder heated to 100°C. A single layer of WSe₂ was similarly exfoliated on PDMS from bulk crystals (acquired from HQgraphene) using blue tape (polyvinyl chloride tape 224PR, Nitto). The WSe₂ flake was stamped on top of the hBN at 70°C before a second layer of few-nanometer-thin hBN was transferred on top at 70°C (37). The structure was annealed before every stamping step in a low-pressure forming

gas atmosphere (10^{-2} bar, 5% H_2 in N_2) at $150^\circ C$ for 2 to 4 hours. Several tens of single nanowires were covered by the resulting vdW stack. We also note that the alternative method of drop-casting nanowires from propan-2-ol solution instead resulted in a compromised optical quality of WSe_2 monolayers.

Optical spectroscopy

The sample was mounted inside a He-flow cryostat (KONTI Cryostat Type Microscope, CryoVac), placed on top of an inverted microscope (Eclipse Ti-U, Nikon), and held under high-vacuum conditions (10^{-8} bar) when measured at low temperatures. For time-integrated μ -PL mapping, we used continuous-wave laser excitation (LRS 0532 PFM, Laserglow Technologies) at the photon energy of 2.33 eV and 0.4 μW power. The laser beam was focused onto the sample to spot diameters of about ~ 1.0 μm using either 60 \times [CFI S Plan Fluor ELWD 60XC, numerical aperture (NA) = 0.7, Nikon] or 100 \times (TU Plan Fluor 100X, NA = 0.9, Nikon) microscope objectives.

The resulting emission from the sample was filtered by a combination of two spectrally tunable filters with a spectrally sharp cutoff edge (VersaChrome Edge, Semrock) to remove both the laser light and the GaAs nanowire PL at 1.52 eV, well below the bandgap of the WSe_2 monolayer. A pinhole with 50 μm diameter was used to spatially filter the resulting PL from the excited region in the image plane before it was directed into a spectrometer (Acton SpectraPro SP-2300, Princeton Instruments) and dispersed onto a charge-coupled device (CCD) (Pixis 256, Princeton Instruments). The full width at half maximum values in Fig. 4 were numerically determined from the spectrally resolved μ -PL line scan. For the linear reflectance spectroscopy measurements presented in note S3, we used the attenuated output of a spectrally broadband tungsten-halogen lamp (250W QTH, Newport) as a light source, spatially filtered and focused by the 60 \times microscope objective onto a spot size of 2.0 μm . The reflected signal was detected by a CCD coupled to a spectrometer.

Time-resolved emission microscopy

For time-resolved emission microscopy measurements, 100-fs pulses with 80-MHz repetition frequency from a tunable Ti:sapphire laser (Chameleon Ultra II, Coherent Inc.) set to operate at 1.77 eV were focused to a spot size of 1.0 μm using the 60 \times (NA = 0.7) glass-corrected objective. To obtain the data in Figs. 2 and 3, an estimated electron-hole pair density of $\sim 10 \times 10^{11} \text{ cm}^{-2}$ was injected by setting the excitation energy density to 5 $\mu J/\text{cm}^2$ per pulse at 0.8% absorption at the high-energy flank of the X_0 resonance (cf. also note S3). To minimize Auger-like exciton-exciton annihilation effects (38), room temperature experiments shown in Fig. 4 were performed at much smaller densities, using 0.5 $\mu J/\text{cm}^2$ per pulse.

A lateral cross section of the resulting PL emission was either directly imaged onto a streak camera (CI0910, Hamamatsu) using a mirror for time- and spatially resolved measurements. For time- and spectrally resolved detection, a 300 mm^{-1} grating was used instead. In spatially resolved measurement, the emission is measured either along (x) or across (y) the nanowire direction by rotating the sample relative to the detector slit. To obtain 2D maps of the time-resolved emission in Fig. 3C, we align the sample in the y direction parallel to the detector slit and subsequently image several cross sections of the PL emission by manually shifting the image plane along the x direction. These data are then combined to a 2D image. For the analysis in Figs. 2 and 4, the emission profiles

are integrated over 100-ps time intervals and fitted by a Gaussian [$\sim \exp(-\mathbf{r}^2/\sigma(t)^2)$] to determine the transient change of the variance, $\Delta\sigma(t)^2 = \sigma(t)^2 - \sigma_0^2$, as a function of time. From $\Delta\sigma(t)^2 = 2Dt$, we obtain the diffusion coefficient D .

Numerical simulation of exciton transport

For numerical simulations, the time evolution of an initial Gaussian exciton density, $n(\mathbf{r},0) = n_0 \exp(-\mathbf{r}^2/2\sigma_0^2)$ with $\sigma_0 = 0.3$ μm , centered on top of the quasi-1D potential $u = u(\mathbf{r})$, was evaluated based on Eq. 1 using a spatial grid of 200 \times 200 points with a step size of 0.04 μm and a temporal resolution below 1 ps. As input, experimentally derived parameters, $D = 1.4 \text{ cm}^2/\text{s}$, $\tau = 300$ ps, and a potential depth of 9 meV, were used. To compare the numerical results with the exciton emission profiles obtained in experiments, the calculated real-space distribution of excitons was convoluted with the point spread function of the objective lens approximated by a Gaussian with a full width at half maximum of ~ 550 nm. Including a position-dependent diffusion coefficient along the y direction in Eq. 1 modifies the drift-diffusion model to account for a strain-dependent diffusivity emerging at elevated temperatures (cf. note S10).

First-principles calculations of strained WSe_2

The first-principles calculations were performed using density functional theory within the WIEN2k (39) software implementation. For the in-plane strain applied to the WSe_2 monolayer, the atomic positions were fully relaxed along the out-of-plane direction. A vacuum region of 20 \AA was considered to avoid the interaction between monolayer replicas. The self-consistent calculations were performed using a Monkhorst-Pack grid with 15 \times 15 k-points, a core-valence energy separation of -6 rydberg (Ry), a plane-wave cutoff multiplied by the smallest atomic radii of 9, and a convergence criteria of $10^{-6} e$ for the charge, 10^{-6} Ry for the energy, and 10^{-1} mRy/bohr for the forces. Spin-orbit coupling was included fully relativistically for core electrons and via a second variational approach for valence electrons (40). We systematically analyze the influence of different exchange-correlation functionals as well as the effect of biaxial and uniaxial strain. To estimate the number of excitonic levels confined in the strained region, we evaluate the Hamiltonian of the exciton center of mass subjected to an external confinement potential. Further details are discussed in notes S2 and S9.

SUPPLEMENTARY MATERIALS

Supplementary material for this article is available at <https://science.org/doi/10.1126/sciadv.abj3066>

REFERENCES AND NOTES

1. D. N. Basov, R. D. Averitt, D. Hsieh, Towards properties on demand in quantum materials. *Nat. Mater.* **16**, 1077–1088 (2017).
2. E. Altman, K. R. Brown, G. Carleo, L. D. Carr, E. Demler, C. Chin, B. DeMarco, S. E. Economou, M. A. Eriksson, K. M. C. Fu, M. Greiner, K. R. A. Hazzard, R. G. Hulet, A. J. Kollár, B. L. Lev, M. D. Lukin, R. Ma, X. Mi, S. Misra, C. Monroe, K. Murch, Z. Nazario, K. K. Ni, A. C. Potter, P. Roushan, M. Saffman, M. Schleier-Smith, I. Siddiqi, R. Simmonds, M. Singh, I. B. Spielman, K. Temme, D. S. Weiss, J. Vučković, V. Vuletić, J. Ye, M. Zwerlein, Quantum simulators: Architectures and opportunities. *PRX Quantum* **2**, 017003 (2021).
3. G. Mazza, M. Rösner, L. Windgätter, S. Latini, H. Hübener, A. J. Millis, A. Rubio, A. Georges, Nature of symmetry breaking at the excitonic insulator transition: Ta_2NiSe_5 . *Phys. Rev. Lett.* **124**, 197601 (2020).
4. L. Ma, P. X. Nguyen, Z. Wang, Y. Zeng, K. Watanabe, T. Tanaguchi, A. H. MacDonald, K. F. Mak, J. Shan, Strongly correlated excitonic insulator in atomic double layers. arXiv:2104.05066 (2021).
5. M. M. Fogler, L. V. Butov, K. S. Novoselov, High-temperature superfluidity with indirect excitons in van der Waals heterostructures. *Nat. Commun.* **5**, 4555 (2014).

6. S. Gupta, A. Kutana, B. I. Yakobson, Heterobilayers of 2D materials as a platform for excitonic superfluidity. *Nat. Commun.* **11**, 2989 (2020).
7. Z. Wang, D. A. Rhodes, K. Watanabe, T. Taniguchi, J. C. Hone, J. Shan, K. F. Mak, Evidence of high-temperature exciton condensation in two-dimensional atomic double layers. *Nature* **574**, 76–80 (2019).
8. L. V. Keldysh, The electron-hole liquid in semiconductors. *Contemp. Phys.* **27**, 395–428 (1986).
9. T. B. Arp, D. Pleskot, V. Aji, N. M. Gabor, Electron–hole liquid in a van der waals heterostructure photocell at room temperature. *Nat. Photonics* **13**, 245–250 (2019).
10. O. Cotlet, S. Zeytinoglu, M. Sigrist, E. Demler, A. Imamoglu, Superconductivity and other collective phenomena in a hybrid bose-fermi mixture formed by a polariton condensate and an electron system in two dimensions. *Phys. Rev. B* **93**, 054510 (2016).
11. M. E. Zhitomirsky, T. M. Rice, V. I. Anisimov, Ferromagnetism in the hexaborides. *Nature* **402**, 251–253 (1999).
12. I. M. Georgescu, S. Ashhab, F. Nori, Quantum simulation. *Rev. Mod. Phys.* **86**, 153–185 (2014).
13. L. Tarruell, L. Sanchez-Palencia, Quantum simulation of the hubbard model with ultracold fermions in optical lattices. *C. R. Phys.* **19**, 365–393 (2018).
14. P. G. Lagoudakis, N. G. Berloff, A polariton graph simulator. *New J. Phys.* **19**, 125008 (2017).
15. N. G. Berloff, M. Silva, K. Kalinin, A. Askitopoulos, J. D. Töpfer, P. Cilibizzi, W. Langbein, P. G. Lagoudakis, Realizing the classical XY Hamiltonian in polariton simulators. *Nat. Mater.* **16**, 1120–1126 (2017).
16. D. M. Kennes, M. Claassen, L. Xian, A. Georges, A. J. Millis, J. Hone, C. R. Dean, D. N. Basov, A. N. Pasupathy, Moiré heterostructures as a condensed-matter quantum simulator. *Nat. Phys.* **17**, 155–163 (2021).
17. L. V. Butov, C. W. Lai, A. L. Ivanov, A. C. Gossard, D. S. Chemla, Towards Bose–Einstein condensation of excitons in potential traps. *Nature* **417**, 47–52 (2002).
18. K. Yoshioka, E. Chae, M. Kuwata-Gonokami, Transition to a Bose–Einstein condensate and relaxation explosion of excitons at sub-Kelvin temperatures. *Nat. Commun.* **2**, 328 (2011).
19. J. Zhang, X. Tan, M. Liu, S. W. Teitelbaum, K. W. Post, F. Jin, K. A. Nelson, D. N. Basov, W. Wu, R. D. Averitt, Cooperative photoinduced metastable phase control in strained manganite films. *Nat. Mater.* **15**, 956–960 (2016).
20. A. Castellanos-Gomez, R. Roldán, E. Cappelluti, M. Buscema, F. Guinea, H. S. J. van der Zant, G. A. Steele, Local strain engineering in atomically thin mos₂. *Nano Lett.* **13**, 5361–5366 (2013).
21. A. Branny, S. Kumar, R. Proux, B. D. Gerardot, Deterministic strain-induced arrays of quantum emitters in a two-dimensional semiconductor. *Nat. Commun.* **8**, 15053 (2017).
22. D. F. Cordovilla Leon, Z. Li, S. W. Jang, C.-H. Cheng, P. B. Deotare, Exciton transport in strained monolayer WSe₂. *Appl. Phys. Lett.* **113**, 252101 (2018).
23. H. Moon, G. Grosso, C. Chakraborty, C. Peng, T. Taniguchi, K. Watanabe, D. Englund, Dynamic exciton funneling by local strain control in a monolayer semiconductor. *Nano Lett.* **20**, 6791–6797 (2020).
24. M. G. Harats, J. N. Kirchof, M. Qiao, K. Greben, K. I. Bolotin, Dynamics and efficient conversion of excitons to trions in non-uniformly strained monolayer WS₂. *Nat. Photonics* **14**, 324–329 (2020).
25. O. B. Aslan, M. Deng, T. F. Heinz, Strain tuning of excitons in monolayer WSe₂. *Phys. Rev. B* **98**, 115308 (2018).
26. I. Niehues, R. Schmidt, M. Drüppel, P. Maruhn, D. Christiansen, M. Selig, G. Berghäuser, D. Wigger, R. Schneider, L. Braasch, R. Koch, A. Castellanos-Gomez, T. Kuhn, A. Knorr, E. Malic, M. Rohlfing, S. Michaelis de Vasconcellos, R. Bratschitsch, Strain control of exciton–phonon coupling in atomically thin semiconductors. *Nano Lett.* **18**, 1751–1757 (2018).
27. F. Carrascoso, H. Li, R. Frisenda, A. Castellanos-Gomez, Strain engineering in single-, bi- and tri-layer MoS₂, MoSe₂, WS₂ and WSe₂. *Nano Res.* **14**, 1698–1703 (2021).
28. K. Zollner, P. E. Faria Junior, J. Fabian, Strain-tunable orbital, spin-orbit, and optical properties of monolayer transition-metal dichalcogenides. *Phys. Rev. B* **100**, 195126 (2019).
29. M. Feierabend, Z. Khatibi, G. Berghäuser, E. Malic, Dark exciton based strain sensing in tungsten-based transition metal dichalcogenides. *Phys. Rev. B* **99**, 195454 (2019).
30. K. Wagner, J. Zipfel, R. Rosati, E. Wietek, J. D. Ziegler, S. Brem, R. Perea-Causin, T. Taniguchi, K. Watanabe, M. M. Glazov, E. Malic, A. Chernikov, Nonclassical exciton diffusion in monolayer WSe₂. *Phys. Rev. Lett.* **127**, 076801 (2021).
31. Z. Khatibi, M. Feierabend, M. Selig, S. Brem, C. Linderälrv, P. Erhart, E. Malic, Impact of strain on the excitonic linewidth in transition metal dichalcogenides. *2D Mater.* **6**, 015015 (2018).
32. R. Rosati, S. Brem, R. Perea-Causin, R. Schmidt, I. Niehues, S. M. de Vasconcellos, R. Bratschitsch, E. Malic, Strain-dependent exciton diffusion in transition metal dichalcogenides. *2D Mater.* **8**, 015030 (2020).
33. J. S. Ross, P. Rivera, J. Schaibley, E. Lee-Wong, H. Yu, T. Taniguchi, K. Watanabe, J. Yan, D. Mandrus, D. Cobden, W. Yao, X. Xu, Interlayer exciton optoelectronics in a 2D heterostructure p–n junction. *Nano Lett.* **17**, 638–643 (2017).
34. Y. Bai, L. Zhou, J. Wang, W. Wu, L. J. McGilly, D. Halbertal, C. F. B. Lo, F. Liu, J. Ardelean, P. Rivera, N. R. Finney, X. C. Yang, D. N. Basov, W. Yao, X. Xu, J. Hone, A. N. Pasupathy, X. Y. Zhu, Excitons in strain-induced one-dimensional moiré potentials at transition metal dichalcogenide heterojunctions. *Nat. Mater.* **19**, 1068–1073 (2020).
35. V. V. Deshpande, M. Bockrath, L. I. Glazman, A. Yacoby, Electron liquids and solids in one dimension. *Nature* **464**, 209–216 (2010).
36. F. Dirnberger, D. Abujetas, J. König, M. Forsch, T. Koller, I. Gronwald, C. Lange, R. Huber, C. Schüller, T. Korn, J. Sánchez-Gil, D. Bougeard, Tuning spontaneous emission through waveguide cavity effects in semiconductor nanowires. *Nano Lett.* **19**, 7287–7292 (2019).
37. A. Castellanos-Gomez, M. Buscema, R. Molenaar, V. Singh, L. Janssen, H. S. J. van der Zant, G. A. Steele, Deterministic transfer of two-dimensional materials by all-dry viscoelastic stamping. *2D Mater.* **1**, 011002 (2014).
38. J. Zipfel, M. Kulig, R. Perea-Causin, S. Brem, J. D. Ziegler, R. Rosati, T. Taniguchi, K. Watanabe, M. M. Glazov, E. Malic, A. Chernikov, Exciton diffusion in monolayer semiconductors with suppressed disorder. *Phys. Rev. B* **101**, 115430 (2020).
39. P. Blaha, K. Schwarz, F. Tran, R. Laskowski, G. K. H. Madsen, L. D. Marks, Wien2k: An APW+lo program for calculating the properties of solids. *J. Chem. Phys.* **152**, 074101 (2020).
40. D. J. Singh, L. Nordstrom, *Planewaves, Pseudopotentials, and the LAPW Method* (Springer Science & Business Media, 2006).
41. Z. Li, T. Wang, C. Jin, Z. Lu, Z. Lian, Y. Meng, M. Blei, S. Gao, T. Taniguchi, K. Watanabe, T. Ren, S. Tongay, L. Yang, D. Smirnov, T. Cao, S.-F. Shi, Emerging photoluminescence from the dark-exciton phonon replica in monolayer WSe₂. *Nat. Commun.* **10**, 2469 (2019).
42. E. Liu, J. van Baren, Z. Lu, M. M. Altairy, T. Taniguchi, K. Watanabe, D. Smirnov, C. H. Lui, Gate tunable dark trions in monolayer WSe₂. *Phys. Rev. Lett.* **123**, 027401 (2019).
43. Z. Li, T. Wang, Z. Lu, M. Khatoniari, Z. Lian, Y. Meng, M. Blei, T. Taniguchi, K. Watanabe, S. A. McGill, S. Tongay, V. M. Menon, D. Smirnov, S. F. Shi, Direct observation of gate-tunable dark trions in monolayer WSe₂. *Nano Lett.* **19**, 6886–6893 (2019).
44. M. He, P. Rivera, D. Van Tuan, N. P. Wilson, M. Yang, T. Taniguchi, K. Watanabe, J. Yan, D. G. Mandrus, H. Yu, H. Dery, W. Yao, X. Xu, Valley phonons and exciton complexes in a monolayer semiconductor. *Nat. Commun.* **11**, 618 (2020).
45. R. Schmidt, I. Niehues, R. Schneider, M. Drüppel, T. Deilmann, M. Rohlfing, S. M. de Vasconcellos, A. Castellanos-Gomez, R. Bratschitsch, Reversible uniaxial strain tuning in atomically thin WSe₂. *2D Mater.* **3**, 021011 (2016).
46. I. Niehues, P. Maruhn, T. Deilmann, D. Wigger, R. Schmidt, A. Arora, S. Michaelis de Vasconcellos, M. Rohlfing, R. Bratschitsch, Strain tuning of the stokes shift in atomically thin semiconductors. *Nanoscale* **12**, 20786–20796 (2020).
47. R. Frisenda, M. Drüppel, R. Schmidt, S. M. de Vasconcellos, D. P. de Lara, R. Bratschitsch, M. Rohlfing, A. Castellanos-Gomez, Biaxial strain tuning of the optical properties of single-layer transition metal dichalcogenides. *npj 2D Mater. Appl.* **1**, 10 (2017).
48. W. Kohn, L. J. Sham, Self-consistent equations including exchange and correlation effects. *Phys. Rev.* **140**, A1133–A1138 (1965).
49. J. P. Perdew, Y. Wang, Accurate and simple analytic representation of the electron-gas correlation energy. *Phys. Rev. B* **45**, 13244–13249 (1992).
50. J. P. Perdew, K. Burke, M. Ernzerhof, Generalized gradient approximation made simple. *Phys. Rev. Lett.* **77**, 3865–3868 (1996).
51. J. P. Perdew, A. Ruzsinszky, G. I. Csonka, O. A. Vydrov, G. E. Scuseria, L. A. Constantin, X. Zhou, K. Burke, Restoring the density-gradient expansion for exchange in solids and surfaces. *Phys. Rev. Lett.* **100**, 136406 (2008).
52. K.-A. N. Duerloo, M. T. Ong, E. J. Reed, Intrinsic piezoelectricity in two-dimensional materials. *J. Phys. Chem. Lett.* **3**, 2871–2876 (2012).
53. A. Kormányos, G. Burkard, M. Gmitra, J. Fabian, V. Zolyomi, N. D. Drummond, V. Fal'ko, kp theory for two-dimensional transition metal dichalcogenide semiconductors. *2D Mater.* **2**, 022001 (2015).
54. S. J. Byrnes, Multilayer optical calculations. arXiv:1603.02720 (2016).
55. A. Raja, L. Waldecker, J. Zipfel, Y. Cho, S. Brem, J. D. Ziegler, M. Kulig, T. Taniguchi, K. Watanabe, E. Malic, T. F. Heinz, T. C. Berkelbach, A. Chernikov, Dielectric disorder in two-dimensional materials. *Nat. Nanotechnol.* **14**, 832–837 (2019).
56. A. V. Stier, N. P. Wilson, K. A. Velizhanin, J. Kono, X. Xu, S. A. Crooker, Magneto-optics of exciton rydberg states in a monolayer semiconductor. *Phys. Rev. Lett.* **120**, 057405 (2018).
57. K. Wagner, E. Wietek, J. D. Ziegler, M. A. Semina, T. Taniguchi, K. Watanabe, J. Zipfel, M. M. Glazov, A. Chernikov, Autoionization and dressing of excited excitons by free carriers in monolayer WSe₂. *Phys. Rev. Lett.* **125**, 267401 (2020).
58. M. Feierabend, A. Morlet, G. Berghäuser, E. Malic, Impact of strain on the optical fingerprint of monolayer transition-metal dichalcogenides. *Phys. Rev. B* **96**, 045425 (2017).
59. D. F. C. Leon, Z. Li, S. W. Jang, P. B. Deotare, Hot exciton transport in WSe₂ monolayers. *Phys. Rev. B* **100**, 241401 (2019).
60. K. Tran, G. Moody, F. Wu, X. Lu, J. Choi, K. Kim, A. Rai, D. A. Sanchez, J. Quan, A. Singh, J. Embley, A. Zepeda, M. Campbell, T. Autry, T. Taniguchi, K. Watanabe, N. Lu,

- S. K. Banerjee, K. L. Silverman, S. Kim, E. Tutuc, L. Yang, A. H. MacDonald, X. Li, Evidence for moiré excitons in van der Waals heterostructures. *Nature* **567**, 71–75 (2019).
61. D. A. Ruiz-Tijerina, I. Soltero, F. Mireles, Theory of moiré localized excitons in transition metal dichalcogenide heterobilayers. *Phys. Rev. B* **102**, 195403 (2020).
62. T. C. Berkelbach, M. S. Hybertsen, D. R. Reichman, Theory of neutral and charged excitons in monolayer transition metal dichalcogenides. *Phys. Rev. B* **88**, 045318 (2013).
63. A. V. Stier, K. M. McCreary, B. T. Jonker, J. Kono, S. A. Crooker, Exciton diamagnetic shifts and valley Zeeman effects in monolayer WS₂ and MoS₂ to 65 tesla. *Nat. Commun.* **7**, 10643 (2016).
64. M. Goryca, J. Li, A. V. Stier, T. Taniguchi, K. Watanabe, E. Courtade, S. Shree, C. Robert, B. Urbaszek, X. Marie, S. A. Crooker, Revealing exciton masses and dielectric properties of monolayer semiconductors with high magnetic fields. *Nat. Commun.* **10**, 4172 (2019).

Acknowledgments: We thank M. M. Glazov for interesting and helpful discussions and I. Gronwald for support with the atomic force microscopy measurements. **Funding:** Work at CUNY was supported through the NSF QII TAQS 1936276 (to F.D.), NSF EPMD: 1906096 (to R.B.), and the Army Research Office MURI grant W911NF-17-1-0312 (to V.M.M.). Work at the University of Regensburg was funded by the Deutsche Forschungsgemeinschaft (DFG, German Research Foundation) through Emmy Noether Initiative (CH1672/1 to A.C.), SFB 1277 (projects B05 and B07 to A.C., D.B., P.E.F.J. and J.F. and project B11 to P.E.F.J. and J.F.), SPP 2244 (CH1672/4-1 to A.C.), SPP 2196 (CH1672/3-1 to A.C.), and Würzburg-Dresden Cluster of

Excellence on Complexity and Topology in Quantum Matter ct.qmat (EXC 2147 to A.C.). The project was also funded by the DFG through Projektnummer 451072703 (to F.D.), K.W. and T.T. acknowledge support from the Elemental Strategy Initiative, conducted by the MEXT, Japan, grant number JPMXP0112101001, JSPS KAKENHI grant number JP20H00354, and the CREST (JPMJCR15F3), JST. **Author contributions:** F.D. and J.D.Z. conceived and realized the experimental idea with input from V.M.M. and A.C., as well as analyzed and interpreted the results. Simulations were performed by J.D.Z. with support from R.B. P.E.F.J. and J.F. performed the first-principles calculations. K.W. and T.T. provided the hBN crystals. F.D. and D.B. synthesized the GaAs nanowires. J.D.Z. and F.D. prepared the 1D/2D structures. All authors contributed to the writing of the manuscript. A.C. and V.M.M. supervised the project. **Competing interests:** The authors declare that they have no competing interests. **Data and materials availability:** All data needed to evaluate the conclusions in the paper are present in the paper and/or the Supplementary Materials.

Submitted 5 May 2021

Accepted 10 September 2021

Published 29 October 2021

10.1126/sciadv.abj3066

Citation: F. Dirnberger, J. D. Ziegler, P. E. Faria Junior, R. Bushati, T. Taniguchi, K. Watanabe, J. Fabian, D. Bougeard, A. Chernikov, V. M. Menon, Quasi-1D exciton channels in strain-engineered 2D materials. *Sci. Adv.* **7**, eabj3066 (2021).